Journal of
Materials Chemistry A

PAPER

View Article Online
View Journal | View Issue

Cite this: *J. Mater. Chem. A*, 2025, **13**, 35480

Received 24th July 2025
Accepted 15th September 2025

DOI: 10.1039/d5ta06004d

rsc.li/materials-a

Assignment of elementary reactions to impedance components for solid-oxide fuel cells and proton-conducting ceramic fuel cells with Yb and Co-doped barium zirconate as the cathode

Yuji Okuyama, *[ab] Tomohiro Nishiya,[b] Yuichi Mikami,[c] Kosuke Yamauchi[d] and Tomohiro Kuroha[c]

To clarify the elementary reactions of multiple impedance components in fuel cell electrodes, the impedance characteristics of Ni anode-supported fuel cells with $BaZr_{0.8}Yb_{0.2}O_{3-\delta}$ and $Zr_{0.84}Y_{0.16}O_{2-\delta}$ electrolytes were evaluated using $BaZr_{0.3}Yb_{0.2}Co_{0.5}O_{3-\delta}$ as the cathode. The elementary reactions were identified by separating impedance components based on isotope effects during proton/deuteron substitution. Distribution of relaxation time analysis showed that the electrode impedances of the proton-conducting ceramic fuel cells (PCFCs) and solid-oxide fuel cells (SOFCs) could be separated into five components. The isotope effect in the impedance was investigated by replacing the anode gas from H_2O-H_2 to D_2O-D_2. For PCFCs, isotope effects appeared in two high-frequency components under open-circuit voltage (OCV), indicating their relation to the anodic reaction; however, isotope effects appeared in the lowest-frequency component under bias (0.85 V). This component was attributable to water vapor formation in PCFCs. By contrast, isotope effects were observed in the three middle-frequency components under bias (0.85 V) in SOFCs, indicating their relation to the anodic reaction; however, no isotope effects appeared in the highest-frequency component among three middle-furequency components under OCV. This component was attributed to water vapor formation in SOFCs.

Introduction

Solid-oxide fuel cells (SOFCs) have been commercialized as stationary fuel cells that use yttria-stabilized zirconia (YSZ) with high oxide ion conductivity as the electrolyte. SOFCs operate at high temperatures of 700°C–1000 °C and exhibit excellent mechanical properties; therefore, they are highly durable. In recent years, proton-conducting ceramic fuel cells (PCFCs) have been actively developed for operation at intermediate temperatures of 500°C–700 °C. PCFCs can deliver high power density and high energy efficiency at 500°C–700 °C.[1–7] Low-temperature operation can reduce material costs and start-up times of PCFCs. In PCFCs, protons traverse through the electrolyte, react with oxygen, and generate steam at the cathode. Therefore, PCFCs can use large amounts of fuel, as the fuel is not diluted by steam.

SOFCs and PCFCs use Ni as the anode and oxygen/electron mixed-conducting oxides such as $La_{0.6}Sr_{0.4}Co_{0.2}Fe_{0.8}O_{3-\delta}$, $La_{0.6}Sr_{0.4}CoO_{3-\delta}$, and $Ba_{0.5}Sr_{0.5}Co_{0.8}Fe_{0.2}O_{3-\delta}$ as cathodes.[8–11] The following elementary reactions possibly occur at the anode and cathode:

Hydrogen oxidation reaction

$$\text{Dissociative adsorption: } H_2(g) \rightarrow 2H_{ad,surf} \quad (1)$$

$$\text{Surface diffusion: } 2H_{ad,surf} \rightarrow 2H_{ad,TPB} \quad (2)$$

$$\text{Charge transfer: } 2H_{ad,TPB} \rightarrow 2H^+ + 2e^- \quad (3)$$

Oxygen reduction reaction

$$\text{Dissociative adsorption: } O_2 \rightarrow 2O_{ad,surf} \quad (4)$$

$$\text{Charge transfer: } O_{ad,surf} + 2e^- \rightarrow O^{2-} \quad (5)$$

Steam production

$$\text{Steam formation: } 2H^+ + O^{2-} \rightarrow H_2O_{ad,TPB} \quad (6)$$

$$\text{Steam desorption: } H_2O_{ad,TPB} \rightarrow H_2O(g) \quad (7)$$

---

[a] Department of Applied Chemistry, Faculty of Engineering, University of Miyazaki, 1-1 Gakuenkibanadai-nishi, Miyazaki 889-2192, Japan. E-mail: okuyama@cc.miyazaki-u.ac.jp

[b] Department of Environmental Robotics, Mechanical Systems and Informatics Course, Graduate School of Engineering, University of Miyazaki, 1-1 Gakuenkibanadai-nishi, Miyazaki 889-2192, Japan

[c] Global Environment Business Development Center, Panasonic Corporation, 3-1-1 Yagumo-naka-machi, Moriguchi City, Osaka, 570-8501, Japan

[d] Device Solutions Business Division, Panasonic Industry Co., Ltd, 25 Kobata-nishinaka, Uji City, Kyoto, 611-8585, Japan

where the subscripts "ad" and "surf" denote adsorption and the electrode surface, respectively, while "TPB" denotes the triple-phase boundary between the electrolyte, electrode, and gas phase. If oxygen reduction and hydrogen oxidation at the electrodes are the rate-limiting steps in fuel cells, PCFCs and SOFCs with identical electrodes will exhibit the same electrode resistance under identical temperature and atmospheric conditions. The impedance of SOFCs and PCFCs has been studied;[12] however, the underlying reaction mechanisms remain unclear because the physical meaning of impedance is not easily interpreted. Elementary electrode reaction mechanisms in SOFCs and PCFCs[12–22] have been analyzed *via* impedance measurements. These analyses observed changes in electrode impedance induced by variations in the partial pressure of the gas used as the active material.[23–29] However, separating multiple elementary reactions based solely on changes in gas concentrations is challenging because partial pressure also determines defect concentration in the electrode and electrolyte.

The cell resistance of SOFCs and PCFCs can be determined *via* impedance analysis. However, impedance spectra may involve overlapping reactions that are difficult to separate and identify. The distribution of relaxation time (DRT) can decompose impedance into different resistance components; however, each elementary reaction cannot be clarified *via* impedance measurements and equivalent circuit analysis alone. Equivalent circuit analysis, commonly used in impedance studies, differs from methods such as *ab initio* modeling that analyze physical motion, including atomic and molecular interactions. It cannot precisely identify elementary reactions at the electrodes of electrochemical cells. Because impedance reflects current, voltage, and time, accurate reaction attribution is impossible when multiple reactions overlap at fuel cell electrodes, unless the rate differences between reactions are clearly understood. To address this issue, this study attempted to identify hydrogen-related impedance components by utilizing differences in hydrogen transport rates *via* the proton/deuteron isotope effect. Furthermore, by comparing the impedances of PCFC and SOFC, we aimed to identify the impedance component associated with the same reaction: oxygen dissociation and adsorption.

We successfully separated cathode and anode impedance components in PCFCs by analyzing the proton/deuteron isotope effect in the polarization resistance of the electrode under open-circuit voltage (OCV) conditions.[19,20] Observations of the isotope effect under polarization further identified the impedance component corresponding to steam formation resistance at the cathode. As the ratio of impedance by the kinetic isotope effect equals the square root of the mass ratio, the hydrogen-related impedance ratio is 1.4 according to the classical oscillation model. This indicates that protons are the major carrier species in the electrode reaction. The same method can be extended to SOFCs for separating cathode and anode impedance components and determining steam formation resistance at the anode.

The objective of this study is to attribute each impedance component of the PCFC cathode to its corresponding elementary reactions and identify the rate-determining reactions at the cathodes of SOFCs and PCFCs. To this end, isotope effects in these fuel cells with the same cathode were employed to separate cathode and anode impedances and identify the impedance components of the steam formation reaction. By comparing these impedance components, common resistance components between the two fuel cells were identified. Finally, the difference in polarization resistance between SOFCs, where oxygen ions are charge carriers, and PCFCs, where protons are charge carriers, using identical electrodes was clarified.

Results and discussion

Performance of PCFCs and SOFCs at medium temperatures (500°C–700 °C)

Ni anode-supported fuel cells with 13 μm-thick $BaZr_{0.8}Yb_{0.2}O_{3-\delta}$ (BZYb) and 15 μm-thick $Zr_{0.84}Y_{0.16}O_{2-\delta}$ (YSZ) electrolytes were separately fabricated *via* tape casting (Fig. 1). In SOFCs, $Ce_{0.8}Gd_{0.2}O_{2-\delta}$ (GDC) was used as a reaction barrier between the cathode and electrolyte. $BaZr_{0.3}Yb_{0.2}Co_{0.5}O_{3-\delta}$ (BZYbCo) with a perovskite structure was used as the cathode in PCFCs and SOFCs. The BZYbCo cathode has a thermal expansion coefficient closely matching that of the BZYb electrolyte, which suppresses peeling and facilitates high cathodic activity in PCFCs.[20] BZYbCo is a mixed oxygen/hole conducting oxide, exhibiting both hole conductivity and oxygen permeability (Fig. S1 and S2). As it lack hydrogen permeability (Fig. S3), cathodic reactions in PCFCs occur at the three-phase boundary between the electrolyte, cathode, and gas phase.

At 500°C–700 °C, PCFCs exhibited higher output than SOFCs (Fig. 2) owing to lower electrolyte resistance in PCFCs resulting from higher ion conductivity of proton-conducting ceramics compared with oxide ion–conducting ceramics within this temperature range (Fig. S4). Impedance measurements showed that the total electrode resistance was higher for SOFCs than for PCFCs at 500°C–700 °C (Fig. S4).

Proton/deuteron isotope effect in the impedance of PCFCs

The impedance components related to hydrogen oxidation and steam formation in PCFCs and SOFCs were determined by

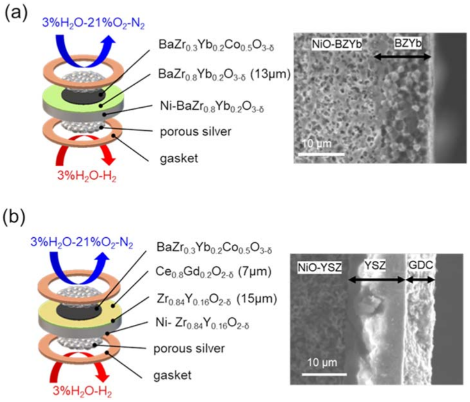

Fig. 1 Cell configuration and cross-sectional images of PCFCs and SOFCs. (a) Anode-supported PCFC using BZYb electrolyte and (b) anode-supported SOFC using YSZ electrolyte.

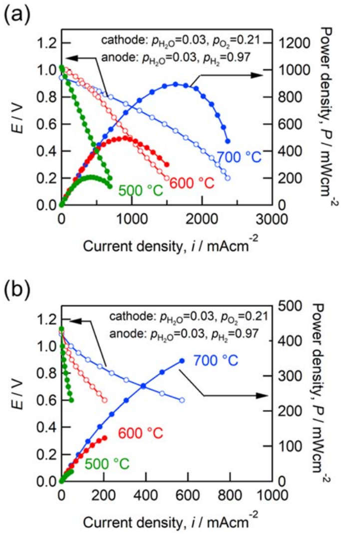

Fig. 2 Performance of PCFCs and SOFCs. (a) Voltage and power density *vs.* current density for PCFCs and (b) voltage and power density *vs.* current density for SOFCs.

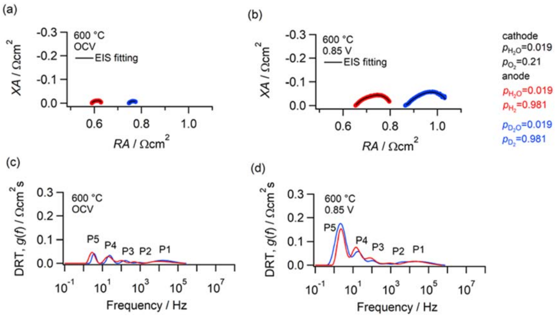

Fig. 4 Nyquist plots and DRT spectra of PCFCs at 600 °C when the gas at the anode is replaced from light hydrogen to heavy hydrogen. Impedance spectra under (a) OCV and (b) polarization states (0.85 V). DRT spectra under (c) OCV and (d) polarization states (0.85 V).

measuring the proton/deuteron isotope effects on electrode resistance under the OCV and polarization states. By measuring changes in impedance components when the gas at the anode switched from H_2O–H_2 to D_2O–D_2 during shutdown and operation of the fuel cells, the impedance components associated with the anodic reaction and steam production reaction at the triple-phase boundary were identified (Fig. 3(a) and (b)). The impedance spectra of Ni anode-supported PCFCs using BZYb as the electrolyte, BZYbCo as the cathode and Ni as the anode were measured at 600 °C *via* the AC two-terminal method (Fig. 4(a) and (b)). The obtained impedances were separated into five electrode impedance components, P1–P5, *via* DRT analysis (Fig. 4(c) and (d)).

The high-frequency intercept with the real axis in the Nyquist plot denotes the resistance of the electrolyte, P0, confirming the isotope effect (Fig. 4(a) and (b)). Here, the ratio of resistance in the isotope effect is <1.41, consistent with the proton transport number of <1 owing to electron leakage.

The isotope effect was confirmed for impedance components P1 and P2 under OCV when the anode gas was changed from H_2O–H_2 to D_2O–D_2 (Table 1), indicating that these high-frequency components corresponding to the anodic reaction.

Under the polarization state (0.85 V), the isotope effect was newly observed for the P5 peak at the lowest frequency (Table 2). In this state, a proton or deuteron traverses the electrolyte, and the isotope effect in resistance arises from the steam formation reaction (Fig. 3(b)). P5 is involved in the cathodic steam formation reaction. No isotope effect was observed on impedance components, P3 and P4, indicating that these middle-frequency components do not participate in hydrogen oxidation or steam formation.

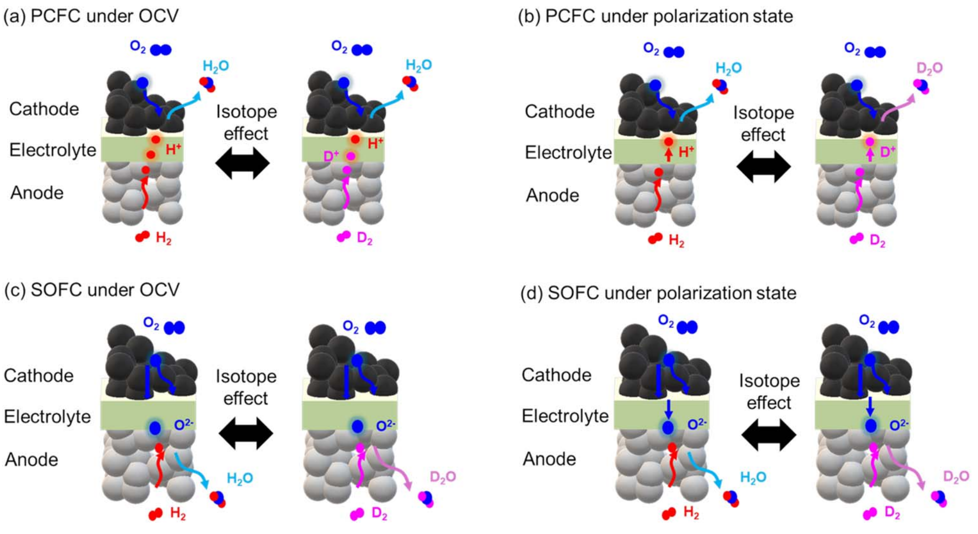

Fig. 3 Schematic of active material movement at the electrodes and ion flow in the electrolyte when anode hydrogen is replaced by deuterium in PCFCs and SOFCs during their shutdown and operation. (a) PCFC at OCV, (b) PCFC under bias, (c) SOFC at OCV, and (d) SOFC under bias.

Table 1 Area-specific resistance (ASR/Ω cm^2) and ratio of isotope effect on the resistance of each component in PCFCs under OCV at 600 °C

OCV	P0	P1	P2	P3	P4	P5
ASR (H_2O–H_2)	0.590	0.014	0.002	0.004	0.013	0.007
ASR (D_2O–D_2)	0.746	0.018	0.003	0.004	0.013	0.007
Ratio (D_2/H_2)	1.266	1.333	1.400	1.000	1.000	1.000

Table 2 Area-specific resistance (ASR/Ω cm^2) and ratio of isotope effect on the resistance of each component in PCFCs under the polarization state (0.85 V) at 600 °C

0.85V	P0	P1	P2	P3	P4	P5
ASR (H_2O–H_2)	0.653	0.025	0.003	0.015	0.028	0.082
ASR (D_2O–D_2)	0.865	0.035	0.004	0.015	0.028	0.112
Ratio (D_2/H_2)	1.325	1.407	1.410	1.000	1.000	1.371

Table 3 Area-specific resistance (ASR/Ω cm^2) and ratio of isotope effect on the resistance of each component for SOFCs under OCV at 600 °C

OCV	P0	P1	P2	P3	P4	P5
ASR (H_2O–H_2)	1.385	0.253	0.116	3.605	0.139	0.863
ASR (D_2O–D_2)	1.394	0.253	0.116	4.326	0.195	0.863
Ratio (D_2/H_2)	1.006	1.000	1.000	1.200	1.407	1.000

Table 4 Area-specific resistance (ASR/Ω cm^2) and ratio of isotope effect on the resistance of each component for SOFCs under the polarization state (0.85 V) at 600 °C

0.85V	P0	P1	P2	P3	P4	P5
ASR (H_2O–H_2)	1.400	0.00001	0.218	0.966	0.071	0.308
ASR (D_2O–D_2)	1.414	0.00001	0.308	1.256	0.100	0.310
Ratio (D_2/H_2)	1.010	1.000	1.410	1.300	1.410	1.005

Proton/deuteron isotope effect in the impedance of SOFCs

In SOFCs, oxide ions flow through the electrolyte and react with hydrogen at the anode to generate steam. As in PCFCs, isotope effects are observed only in the anode resistance of SOFCs when hydrogen at the anode is replaced by deuterium (Fig. 3(c)). Under polarization, isotope effects appear in the resistance associated with the water vapor formation reaction involving oxide ions and hydrogen from the electrolyte (Fig. 3(d)).

The impedance spectra of Ni anode-supported PCFCs using YSZ, GDC, BZYbCo, Ni as the electrolyte, interlayer, cathode, and anode, respectively, were measured at 600 °C *via* the AC two-terminal method (Fig. 5(a) and (b)). The obtained impedances of SOFCs were separated into five electrode impedance components, P1–P5, *via* DRT analysis (Fig. 5 (c) and (d)).

The highest frequency intercept with the real axis in the Nyquist plot is the resistance of the electrolyte, P0, which showed no isotope effect in SOFCs, as observed in PCFCs (Fig. 5(a) and (b)), because the ions moving in the electrolyte were oxide ions rather than protons.

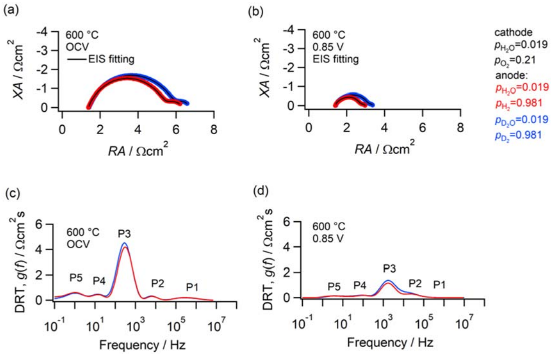

Fig. 5 Nyquist plots of the impedance and DRT spectra of SOFCs at 600 °C when the gas at the anode is replaced from light to heavy hydrogen. Impedance spectra under (a) OCV and (b) polarization states (0.85 V). DRT spectra under (c) OCV and (d) polarization states (0.85 V).

When the anode gas was changed from H_2O–H_2 to D_2O–D_2 under OCV, the isotope effect in SOFCs was confirmed based on the impedance components P3 and P4 in the mid-frequency range (Table 3), indicating that these peaks arise from the anodic reaction.

Under polarization (0.85 V), the isotope effect was newly observed for the P2 peak in the middle-frequency range (Table 4). Under the polarization state, oxide ions traversed the electrolyte and reacted with hydrogen or deuterium at the anode, producing an isotope effect in resistance (Fig. 3(d)). Therefore, P2 corresponds to the component involved in the anodic steam formation reaction in SOFCs. No isotope effect was observed on impedance components P1 and P5, indicating that these components do not participate in the hydrogen oxidation and steam formation reactions.

Current dependence of the impedance of PCFCs and SOFCs

The polarization resistances of PCFCs and SOFCs changed as the cell voltage decreased. Interestingly, the polarization resistance of PCFCs increased while that of SOFCs decreased with decreasing cell voltage, indicating their different voltage dependencies (Fig. 6(a) and (b)). DRT analysis revealed that their impedances could be separated into five components under each polarization state (Fig. 6(c) and (d)), corresponding to cathode and anode impedance components revealed *via* isotope effects. Additionally, components related to the steam formation reaction were identified.

The relaxation times for each impedance process increase in the order of bulk, grain boundary, and electrode reaction. Therefore, using a Nyquist plot, high-frequency components of the impedance can be attributed to fast processes, such as ionic migration in the electrolyte and ohmic resistance, while the low-frequency components corresponds to slow processes at the electrode–electrolyte interface, such as charge transfer kinetics, diffusion, and adsorbate relaxation.

The resistance at the minimum reactance point in the high-frequency region was adopted as the electrolyte resistance (P0).

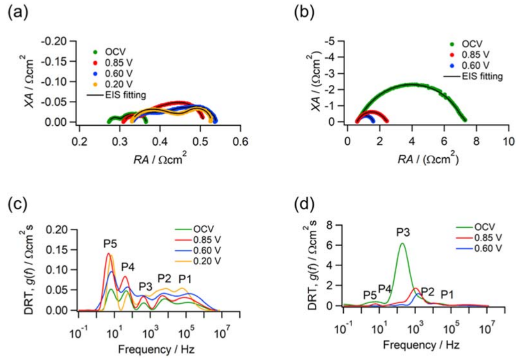

Fig. 6 Nyquist plots and DRT spectra of PCFCs and SOFCs at 600 °C under various polarization states. Impedance spectra of (a) PCFCs and (b) SOFCs. DRT spectra of (c) PCFCs and (d) SOFCs.

In SOFCs, the resistance component P0 (ohmic resistance) of the electrolyte was independent of current density and higher than that in PCFCs (Fig. 7(a)). In PCFCs, the resistance component P0 of the electrolyte increased with current density at low current densities, however, this dependence disappeared at high current densities. This behavior arises from electron leakage: under high oxygen partial pressures, the electrolyte in PCFCs exhibits hole conductivity, causing electron leakage at low current densities.[30] This hole conduction reduced the apparent electrolyte resistance. During fuel cell operation, the oxygen potential distribution within the electrolyte decreases under current flow, rendering electron leakage negligible and leaving the electrolyte resistance governed solely by proton conductivity.

The area-specific resistance (ASR) of P5, which is the resistance component of the steam formation reaction at the cathode in PCFCs, and P4, which is the resistance component of the cathode, depended on current density (Fig. 7(b) and (c)). This trend was similar to that of the aforementioned electrolyte resistance, with apparent resistance presumably reduced owing to electron leakage.

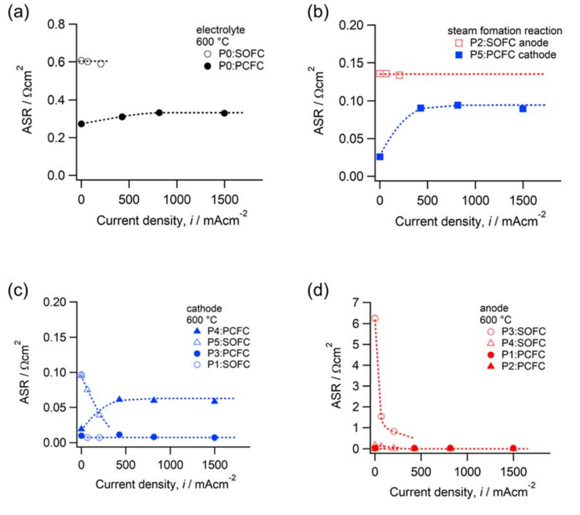

Fig. 7 Current density dependence of the ASR for (a) electrolyte, (b) steam formation reaction, (c) cathode, and (d) anode in PCFCs and SOFCs.

The ASR of the steam formation reaction in PCFCs was smaller than in SOFCs (Fig. 7(b)), indicating that protons are more easily oxidized at 600 °C than oxide ions are reduced.

The ASR of cathode component P3 in PCFCs and cathode component P1 in SOFCs were comparable, as these components correspond to the reactions common to both cells, likely related to oxygen dissociation, adsorption, and dissolution.

Cathode component P4 in PCFCs is a resistance component associated with electron leakage, as evidenced by its current density dependence. As it does not match a cathode component in SOFCs, it likely reflects the oxygen reduction reaction that occurred only on the cathode surface. By contrast, the cathode component P5 of SOFCs decreases with current density and is smaller than P4 in PCFCs. In SOFCs, unlike PCFCs, oxide ions can flow through the cathode and react beyond the triple-phase boundary. P5 thus relates to the transport of oxides within the cathode and reaction resistance at the double-phase boundary between the electrolyte and cathode. As oxygen potential decreases with increasing current density, the concentration of oxide ion vacancies within the cathode increases, explaining the observed decrease in the resistance with current density and confirming the influence of oxide ion transport within the cathode.

The anode components P1 and P2 of PCFCs showed no dependence on current density (Fig. 7(d)). By contrast, the anode components P3 and P4 of SOFCs depended on current density (Fig. 7(d) and S5). In particular, the large resistance of component P3 limited SOFC output at medium temperatures. As isotope effects were observed for all components, they were confirmed as hydrogen-related reaction components. However, further detailed assignment of the anode components in PCFCs and SOFCs is challenging. In PCFCs, reactions related to hydrogen dissociation, adsorption, diffusion, and hydrogen oxidation occurred undoubtedly. By contrast, in SOFCs, the ASR dependence of current density indicates that steam generated at the anode may contribute to the anodic reaction. The difference in the behavior of the anode impedance components between PCFCs and SOFCs is attributable to the absence of steam. Herein, anode–electrolyte delamination in SOFCs occurred at 700 °C under a voltage of ≤0.5 V, indicating that steam oxidation likely occurred at the Ni anode. This warrants further investigation of the anodic reaction mechanism in SOFCs.

Elementary reaction of the anode for PCFCs and SOFCs

The elementary reactions of anode impedance components P1 and P2 observed in PCFCs were analyzed. Impedance components P1 and P2 show isotope effects but no bias dependence, suggesting that their resistance arises from hydrogen dissociation, adsorption, surface diffusion, and hydrogen oxidation (eqn (8)–(10), red arrow in Fig. 8(a)).

$$H_2(g) \rightarrow 2H_{(ad,suf.)} \tag{8}$$

$$2H_{(ad,suf.)} \rightarrow 2H_{(ad,TPB)} \tag{9}$$

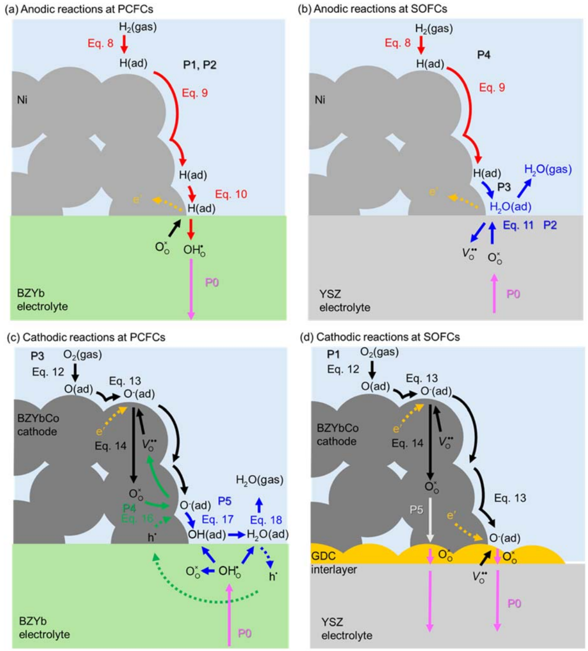

Fig. 8 Anodic reactions in (a) PCFCs and (b) SOFCs. Cathodic reaction in (c) PCFCs and (d) SOFCs.

$$2H_{(ad,TPB)}+2O_O^{\times}\rightarrow 2OH_O^{\bullet}+2e' \tag{10}$$

Here, charge carriers in the electrolyte and electrodes are denoted using Kröger–Vink notation. Hydrogen dissociates and absorbs on the Ni metal surface, diffuses across it, reaches the three-phase boundary, is oxidized, and then dissolves into the electrolyte. These impedance components of PCFC exhibit resistance values close to those of P4 in SOFC. Therefore, the P4 component in SOFC, can be regarded as corresponding to reactions common to PCFCs and SOFCs in eqn (8) and (9) (red arrow in Fig. 8(a) and (b)).

Impedance component P2 in SOFCs can be explained based on isotope effects (blue arrow in Fig. 8(b)).

$$O_O^{\times}+2H_{(ad,TPB)}\rightarrow H_2O_{(ad)}+V_O^{\bullet\bullet}+2e' \tag{11}$$

As this component shows isotope effects only under bias, it is attributable to the resistance of oxide ions flowing through the electrolyte and reacting with adsorbed hydrogen at the three-phase boundary to generate steam.

The elementary reaction of the P3 component in SOFCs remains unidentified. This component differs significantly from the anodic reaction in PCFCs and is presumed to involve in steam generated at the anode, which is unique to SOFCs.

Elementary reaction of the cathode for PCFCs and SOFCs

In PCFCs, oxygen dissociates and adsorbs on the BZYbCo surface, diffuses across its, is reduced, and then reacts with protons from the electrolyte at the three-phase boundary to form water vapor. The elementary reactions of cathode impedance components P3, P4, and P5 observed in PCFCs were analyzed. As no isotope effect was observed for impedance components P3 and P4, the corresponding reactions are not hydrogen-related. As the impedance component P3 has the same resistance as P1 in SOFCs, it likely corresponds to oxygen dissociation, adsorption, and dissolution at the cathode surface (eqn (12)–(14), black arrow in Fig. 8(c) and (d)).

$$O_2(g)\rightarrow 2O_{(ad)} \tag{12}$$

$$2O_{(ad)}+2e'\rightarrow 2O_{(ad)}{}^{-} \tag{13}$$

$$2O_{(ad)}{}^{-}+2V_O^{\bullet\bullet}+2e'\rightarrow 2O_O^{\times} \tag{14}$$

Summarizing these reactions, impedance component P3 in PCFCs can be expressed as follows (eqn (15)):

$$O_2(g)+2V_O^{\bullet\bullet}+4e'\rightarrow 2O_O^{\times}. \tag{15}$$

Impedance component P4 in PCFCs depends on current density, with resistance decreasing at low currents owing to electron leakage (Fig. 7(c)), suggesting that the following reaction is promoted by electron leakage (green arrow in Fig. 8(c)).

$$2O_O^{\times}+2h^{\bullet}\rightarrow 2O_{(ad)}{}^{-}+2V_O^{\bullet\bullet} \tag{16}$$

Impedance component P5 in PCFCs is explained using isotope effects (blue arrow in Fig. 8(c)).

$$2O_{(ad)}{}^{-}+2OH_O^{\bullet}\rightarrow 2OH_{(ad)}+2O_O^{\times} \tag{17}$$

$$2OH_{(ad)}+2OH_O^{\bullet}\rightarrow 2H_2O_{(ad)}+2O_O^{\times}+2h^{\bullet} \tag{18}$$

The remaining SOFC impedance component, P5, is highly dependent on current density. An increase in current density enhances oxygen permeation through the cathode owing to an increase in the oxide ion vacancies at the cathode, possibly decreasing resistance (white arrow in Fig. 8(d)).

The cathode resistance of PCFCs with BZYbCo is low during oxygen dissociation, adsorption, and dissolution, whereas it is highest during the steam formation reaction or proton oxidation reaction. This highlights that reducing the resistance related to steam generation is necessary to improve the power density of PCFC.

BZYbCo is considered an excellent cathode material for SOFCs because of its low resistance during oxygen dissociation, adsorption, and dissolution. Conversely, reducing anode resistance, along with reducing electrolyte resistance, is crucial for achieving low-temperature operation of SOFCs at 600 °C.

Experimental methods

Sample synthesis and cell fabrication

Ni anode-supported planar cells were fabricated *via* tape casting, similar to methods employed for ceramic electronic device fabrication, followed by anode–electrolyte cofiring, as employed for SOFC fabrication. A green sheet for the electrolyte membrane was generated using either the proton-conductive electrolyte material BZYb or the oxygen ion-conductive electrolyte material YSZ (Tosoh, 8-YSZ). First, the electrolyte material was mixed with polyvinyl butyral, butylbenzyl phthalate, and a solvent mixture of butyl acetate and 1-butanol. Polyvinyl butyral and butylbenzyl phthalate functioned as a resin and a plasticizer, respectively, for the binder resin, producing a ceramic slurry. This slurry was applied to a support film *via* tape casting to grow the electrolyte membrane stacked on a support film, yielding the desired green sheet.

A green sheet for the anode was prepared similarly by adding NiO to the mixture used for manufacturing the green sheet. These sheets were stacked to a thickness of 600–800 μm, yielding the desired stacked structure for the anode.

Anode-supported planar cells were fabricated by stacking the electrolyte membrane on the anode and pressing at 353 K and 50 MPa using a hot press. The pressed stacked structure was cut into circular disks of Ø15–30 mm and sintered at 1723 K for 5 h to form the anode-supported planar cells. Furthermore, $Gd_{0.2}Ce_{0.8}O_{2-\delta}$ was spin-coated onto the YSZ electrolyte surface of the SOFC as a reaction prevention layer of the cathode and fired at 1523 K for 2 h.

BZYbCo powder was synthesized *via* a chemical solution method using nitrates as starting materials.[19] BZYbCo paste was applied to the electrolyte surface by screen printing and sintered at 1173 K for 1 h in air. This process produced a fuel cell comprising a cathode, electrolyte membrane, and anode. The sintered anode-supported planar cells with cathode had an external circular diameter of Ø13–20 mm, a cathode diameter of Ø6 or Ø10 mm, an electrolyte thickness of 13–15 μm, and an anode thickness of 600 μm. The anode support film was formed by mixing the electrolyte and NiO in a 2 : 8 volume ratio (Fig. S6).

Impedance analysis

A schematic view of the experimental apparatus is shown in Fig. 9(a) and (b). Wet hydrogen gas ($3\%H_2O–H_2$, $1.9\%H_2O–H_2$ or $1.9\%D_2O–D_2$) and wet air ($3\%H_2O–21\%O_2–N_2$, $1.9\%H_2O–21\%O_2–Ar$) were channeled into the anode and cathode chambers, respectively. The ratio of Ar or N_2 to O_2 in the gas mixtures was controlled by a mass flow controller within ±1%. The activity of water vapor (H_2O or D_2O) in a gas atmosphere was controlled by equilibrating the gas in a thermostatic bath held at the appropriate temperature. The $D_2O–D_2$ mixed gas was prepared using deuterium oxide (99.9% purity, Sigma-Aldrich Corporation) and D_2 gas (99.6% purity, Taiyo Nippon Sanso JFP Corporation). The apparatus has separate gas lines for $H_2O–H_2$ and $D_2O–D_2$, preventing mixing between $H_2O–H_2$ and $D_2O–D_2$. These gases could be switched using a valve without cross-contamination.

To confirm isotope effects in impedance, the cell was set up in the apparatus shown in Fig. 9(a). Ag ink (Nexceris) and Ag mesh served as current collectors for both electrodes. A glass ring, melted at 900 °C for 1 h, formed the glass seals between the air and hydrogen electrodes. The temperature was then lowered to 700 °C, and the anode supply gas was gradually switched from N_2 to H_2 to reduce NiO. Finally, the temperature was lowered to 600 °C, and cell characteristics were evaluated.

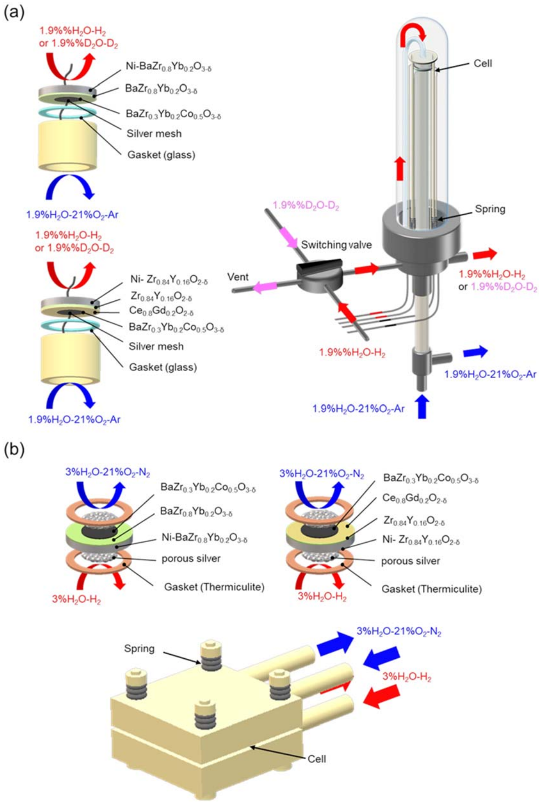

Fig. 9 Schematic view of the experimental apparatus. (a) Isotope Exchange experiment, (b) evaluation of fuel cell performance.

Cell characterization was performed using an alumina cell holder (Chino), as shown in Fig. 9(b). Thermiculite®#866 (Frexitallic) served as the gas seal material. Ag ink (Nexceris) and Ag foam were used as current collectors for both anodes and cathodes. After cell assembly, the temperature was first increased to 700 °C while supplying $3\%H_2O–21\%O_2–N_2$ to the cathode and $3\%H_2O–97\%N_2$ to the anode at 100 cc min^{-1} to sinter the Ag ink. The anode gas was then gradually switched from N_2 to H_2 to reduce NiO. The temperature was then lowered to 600 °C, and cell characteristics were evaluated.

To confirm the isotope effect in electrode impedance, complex impedance was measured under OCV and a bias of 0.85 V at a frequency range of 0.1 Hz–3 MHz using an impedance analyzer (BioLogic VSP-300) at 873 K. Impedances and cell voltages were measured at various current densities (0–1500 mA cm^{-2}).

DRT analysis was performed using Z-Assist software (Toyo Corp.). The real part of impedance was used for DRT analysis to minimize measurement errors and inductive components relative to the imaginary parts. Then, parameters were refined *via* complex nonlinear least squares fitting using EC-Lab software (BioLogic). The equivalent circuit model used for fitting

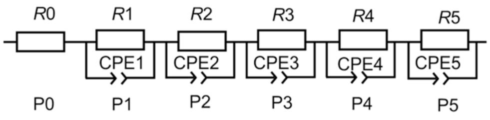

Fig. 10 Equivalent circuit.

assumed a series connection of resistance and parallel resistance–constant phase elements, as shown in Fig. 10.

Conclusions

Herein, hydrogen-related electrode resistance was identified, and impedance components of PCFCs and SOFCs were successfully separated into anode and cathode based on isotope effects of proton and deuterium substitutions. Furthermore, by investigating isotope effects under bias, impedance components attributable to the steam generation reaction were identified.

By comparing electrode resistances of PCFCs and SOFCs that used BZYbCo as the cathode, reactions related to oxygen dissociation, adsorption, and dissolution at the cathode were identified as common resistance components in both fuel cells.

Anode resistance associated with hydrogen adsorption and dissociation on Ni in PCFCs and hydrogen oxidation at the triple-phase boundary was lower than cathode resistance. By contrast, anode resistance is mainly found to reduce the power density of SOFC to a lower value than that of PCFC at 600 °C. In SOFCs, water vapor generated at the triple-phase boundary likely prevents hydrogen diffusion and increases resistance.

Cathode resistance in PCFCs owing to proton oxidation and oxygen reduction reactions decreased at low current densities because of electron leakage, which reduces energy efficiency but lowers electrode resistance. At 600 °C, resistance related to oxygen dissociation, adsorption, and dissolution in BZYbCo was lower than for other electrode reactions, whereas the oxidation reaction of protons exhibited the highest resistance in PCFCs. A proton, the nucleus of a hydrogen atom, requires a strong reducing agent capable of donating electrons to drive the reaction that produces steam. In SOFCs, cathode resistance is expected to be lower than in PCFCs owing to the larger electrode reaction field enabled by the oxide ion conductivity in BZYbCo. To further reduce electrode resistance in PCFCs, imparting proton conductivity to the cathode is necessary to expand the electrode reaction field.

Author contributions

Yuji Okuyama: conceptualization, methodology, validation, formal analysis, investigation, writing – original draft, review and editing, supervision. Tomohiro Nishiya: investigation, formation analysis. Yuichi Mikami: investigation. Kosuke Yamauchi: investigation. Tomohiro Kuroha: supervision.

Conflicts of interest

There are no conflicts to declare.

Data availability

The data that support the findings of this study are available from the corresponding author, [YO], upon reasonable request.

The data supporting this article have been included as part of the SI. This data includes oxygen permeation, hydrogen permeation, and partial conductivity of BZYbCo, impedance spectra of SOFC and PCFC, a photograph of an anode-supported cell. Supplementary information is available. See DOI: **https://doi.org/10.1039/d5ta06004d**.

Acknowledgements

This work was partially supported by NEDO project (JPNP20003) and GteX program (JPMJGX23H).

References

1 C. Duan, J. Tong, M. Shang, S. Nikodemski, M. Sanders, S. Ricote, A. Almansoori and R. O. '. Hayre, *Science*, 2015, **349**, 1321–1326.

2 H. An, H.-W. Lee, B.-K. Kim, Ji-W. Son, K. J. Yoon, H. Kim, D. Shin, H.-l. Ji and J.-Ho Lee, *Nat. Energy*, 2018, **3**, 870–875.

3 K. Bae, D. Y. Jang, H. Jong Choi, D. Kim, J. Hong, B.-K. Kim, J.-H. Lee, J.-W. Son and J. H. Shim, *Nat. Commun.*, 2017, **8**, 14553.

4 S. Choi, C. J. Kucharczyk, Y. Liang, X. Zhang, I. Takeuchi, H.-l. Ji and S. M. Haile, *Nat. Energy*, 2018, **3**, 202–210.

5 S. Choi, T. C. Davenport and S. M. Haile, *Energy Environ. Sci.*, 2019, **12**, 206–215.

6 A. Dubois, S. Ricote and R. J. Braun, *J. Power Sources*, 2017, **369**, 65–77.

7 Y. Matsuzaki, Y. Tachikawa, T. Somekawa, T. Hatae, H. Matsumoto, S. Taniguchi and K. Sasaki, *Sci. Rep.*, 2015, **5**, 12640.

8 C. Sun, *Inorg. Chem. Front.*, 2024, **11**, 8164–8182.

9 H. Shimada, Y. Yamaguchi, H. Sumi and Y. Mizutani, *Ceram. Int.*, 2021, **47**, 16358–16362.

10 H. Shimada, Y. Yamaguchi, H. Sumi and Y. Mizutani, *J. Electrochem. Soc.*, 2020, **167**, 124506.

11 Z. Shao and S. M. Haile, *Nature*, 2004, **431**, 170–173.

12 H. Sumi, H. Shimada, Y. Yamaguchi, Y. Mizutani, Y. Okuyama and K. Amezawa, *Sci. Rep.*, 2021, **11**, 10622.

13 S. M. Choi, H. An, K. J. Yoon, B.-K. Kim, H.-W. Lee, J.-W. Son, H. Kim, D. Shin, H.-I. Ji and J.-H. Lee, *Appl. Energy*, 2019, **233**, 29–36.

14 S. Sun and Z. Cheng, *J. Electrochem. Soc.*, 2017, **164**, 3104–3113.

15 F. He, D. Song, R. Peng, G. Meng and S. Yang, *J. Power Sources*, 2010, **195**, 3359–3364.

16 F. He, T. Wu, R. Peng and C. Xia, *J. Power Sources*, 2009, **194**, 263–268.

17 P. Batocchi, F. Mauvy, S. Fourcade and M. Parco, *Electrochim. Acta*, 2014, **145**, 1–10.

18 H. Sumi, H. Shimada, K. Watanabe, Y. Yamaguchi, K. Nomura, Y. Mizutani, R. M. Matsuda, M. Mori, K. Yashiro, T. Araki and Y. Okuyama, *J. Power Sources*, 2023, **582**, 233528.

19 Y. Okuyama, K. Kasuga, M. Shimomura, Y. Mikami, K. Yamauchi, T. Kuroha and H. Sumi, *J. Power Sources*, 2023, **586**, 233647.

20 Y. Mikami, T. Goto, H. Asano, K. Kasuga, K. Yamauchi, T. Kuroha and Y. Okuyama, *J. Power Sources*, 2024, **613**, 234832.

21 H. Sumi, H. Shimada, K. Watanabe, Y. Yamaguchi, K. Nomura, Y. Mizutani and Y. Okuyama, *ACS Appl. Energy Mater.*, 2023, **6**, 1853–1861.

22 H. Sumi, T. Ohshiro, M. Nakayama, T. Suzuki and Y. Fujishiro, *Electrochim. Acta*, 2015, **184**, 403–409.

23 F. He, T. Wu, R. Peng and C. Xia, *J. Power Sources*, 2009, **194**, 263–268.

24 D.-K. Lim, Ji-H. Kim, A. U. Chavan, T.-R. Lee, Y.-S. Yoo and S.-J. Song, *Ceram. Int.*, 2016, **42**, 3776–3785.

25 J. Jing, Z. Lei, Z. Zheng, H. Wang, P. Zhang, Z. Wang, H. Xu and Z. Yang, *Int. J. Hydrogen Energy*, 2023, **48**, 9037–9045.

26 C.-Y. Yoo., D. S. Yun, S.-Y. Park, J. H. Joo, H. Park, M. Kwak and J. Haeng Yu, *Electrocatalysis*, 2016, **7**, 280–286.

27 K. Xu, H. Zhang, Y. Xu, F. He, Y. Zhou, Y. Pan, J. Ma, B. Zhao, W. Yuan, Y. Chen and M. Liu, *Adv. Funct. Mater.*, 2022, **32**, 2110998.

28 J. Wang, Z. Li, W. Chen, L. Sun, C. Sun and S. Pemg, *Small*, 2025, **21**, e09293.

29 W. Jialu, F. Mi, W. Zhang and C. Sun, *Int. J. Hydrogen Energy*, 2925, **122**, 180–191.

30 Y. Okuyama, Y. Harada, K. Yamauchi, Y. Mikami, T. Kuroha, H. Shimada, Y. Yamaguchi and Y. Mizutani, *J. Electrochem. Soc.*, 2023, **170**, 084509.